Effects of time-energy correlation strength in molecular entangled photon spectroscopy

Fabiano Lever [⬤],[1] Sven Ramelow,[2] and Markus Gühr[1,*]

[1]*Institut für Physik und Astronomie, Universität Potsdam, 14476 Potsdam, Germany*
[2]*Institut für Physik, Humboldt-Universität zu Berlin, 12489 Berlin, Germany*

In this paper, we explore the time-energy domain quantum-classical transition comparing a classical pump-probe experiment on a diatomic molecule to its quantum enhanced counterpart, where the pump and probe pulses are substituted by the signal and idler beams of a spontaneous parametric down conversion (SPDC) source. Absorption of biphotons generated with SPDC exploits quantum time-energy entanglement to enhance the overall yield and selectivity of the process, when compared with a classical pump-probe setup, while maintaining femtosecond time resolution. We systematically study the effects of correlation strength on process efficiency and selectivity, comparing the results to classical pump-probe spectra. An excitation scheme to improve the yield based on spectral narrowing of biphotons is shown. The results indicate that the quantum improvements in yield are caused by a more efficient use of the total power available for the process.

I. INTRODUCTION

Pump-probe spectroscopy [1,2] is a well-known method for the investigation of time-dependent phenomena across a wide range of samples. Two pulse pump-probe spectroscopy relies on a couple of subsequent laser pulses interacting with matter, with the first "pump" pulse exciting the studied system and the second "probe" pulse extracting information about it after a known time delay. This method allows one to study the internal dynamics of the sample in between the two pulses, by observing the changes in an observable as a function of pump-probe delay. A typical pump-probe experiment might study the vibrational or electronic state dynamics of a molecule by inducing a vibrational wave packet with the pump pulse and observing the changes in the absorption of the probe pulse [2].

When using ultrafast pulses, the Fourier uncertainty relation generally imposes a tradeoff between energy and time resolution. Moreover, the two-photon nature of the interaction leads to quadratic power scaling [3] with overall laser intensity, requiring high pulse intensities. Both these issues can be solved by using time-energy entangled photons as pump and probe, allowing for high temporal and spectral resolution as well as linear power scaling [4–6].

Correlated photons can be obtained from spontaneous parametric down conversion (SPDC) [7,8], a nonlinear process in which one photon is converted in a pair of entangled photons (called signal and idler) that have a combined energy equal to the one of the initial photon. With appropriate phase matching, the down conversion can happen for many signal-idler energy pairs [9], allowing for broadband signal and idler photon spectra while maintaining a well-defined total energy. A theoretical analysis of entangled two-photon absorption (ETPA) can be found in [2,8,10–15].

Experimental results in this field focused on the nonresonant case, where the signal and idler light interacts with a short-lived virtual state. In this case, TPA is possible only for signal-idler delays smaller than the virtual state lifetime. Rubidium atoms have been targeted using cavity-enhanced down conversion as a source of correlated photons [5], showing a linear power scaling for the two-photon process when the signal-idler delay is set to zero. Similar results have been obtained on large organic molecules [6,16–18] with energy-degenerate photons obtained from SPDC.

Previous numerical simulations on both resonant and nonresonant ETPA [19–25] have shown how ETPA can be used to increase yield when compared to classical TPA. This paper expands previous analyses with a systematic study of the effects of correlation strength on total yield and ultrafast pump-probe spectra. In addition we present an excitation scheme to further improve yield based on spectral narrowing of biphotons.

II. MODEL

A. System structure

The modeled system consists of a diatomic molecule interacting with a photon field. The molecule is described by a collection of Morse oscillators that represent different electronically excited states. The phase space of the molecule is therefore composed of the various vibronic states that each electronic state supports. The molecule is prepared in the ground vibrational level $|g\rangle$ and undergoes transitions to the intermediate and final electronic states $|i\rangle$ and $|f\rangle$ after interaction with the photons. Since the implemented interaction Hamiltonian does not include any coupling between vibronic states that could lead to population transfer within the ground-state levels, only one ground-state vibrational level is included. This also eliminates the possibility of Raman transitions within the ground state. For the intermediate and
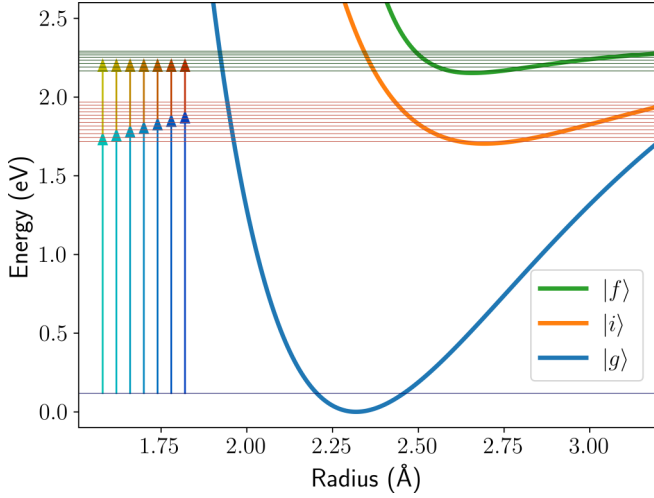
*mguehr@uni-potsdam.de

FIG. 1. Vibrational energy states of the molecule (thin lines) used in the numerical implementation. Only one ground-state level is considered together with the relevant intermediate and final vibronic states (states lying outside the biphoton bandwidth are omitted). Thick lines show the Morse potentials for the internuclear distance in the electronic states. The vertical arrows correspond to different pairs of signal-idler splitting. All possible pairs are coherently superimposed in the correlated state obtained from SPDC.

final states, only vibronic states lying in the biphoton bandwidth are included. The state structure used is represented in Fig. 1.

Although the results presented in this paper are based on numerical values for X, A, and B states (corresponding to $|g\rangle$, $|i\rangle$, and $|f\rangle$, respectively) of ICl from [26], the analysis of the results can be easily generalized to any system with a similar level structure, such as quantum well structures [27,28] or quantum dots [29,30]. It must be, however, noted that the B state of ICl shows predissociation to the 0^+ state [31], which is not included in the model and would lead to decoherence effects and degradation of the efficiency of the process studied.

The molecule interacts with the signal and idler photons sequentially. After the signal photon induces a $|g\rangle \rightarrow |i\rangle$ transition, the molecule evolves unperturbed for a variable time Δt after which the idler photon completes the transition and promotes the molecule to $|f\rangle$.

The biphoton state is described in the energy basis, allowing for an immediate representation of the energy anticorrelation of down converted light. Only two-photon correlations are represented, with no higher-order contributions that are naturally present in an SPDC source with high pump intensities. Letting $|0\rangle$ be the electromagnetic field vacuum state and labeling with $|k_1, k_2\rangle := a_{k_1}^\dagger a_{k_2}^\dagger |0\rangle$ a biphoton state with energies k_1 and k_2, we can describe any correlated state $|\phi\rangle$ by a two-photon wave function $\phi(k_1, k_2)$:

$$|\phi\rangle = \int \phi(k_1, k_2) |k_1, k_2\rangle \, dk_1 dk_2. \tag{1}$$

A state with central energies $\bar{k}_1$, $\bar{k}_2$ and arrival times t_1, t_2 is constructed as

$$\phi(k_1, k_2) = N \exp\left[-\frac{(\Delta k - \Delta\bar{k})^2}{2\sigma_{\text{DC}}^2}\right] \exp\left[-\frac{(\Sigma k - \Sigma\bar{k})^2}{2\sigma_p^2}\right]$$

$$\times \exp\left[-\frac{i}{\hbar}(t_1 k_1 + t_2 k_2)\right] \tag{2}$$

where $\Delta k = k_1 - k_2$ and $\Sigma k = k_1 + k_2$ (and similarly for $\Delta\bar{k}$, $\Sigma\bar{k}$). σ_p is the spectral bandwidth corresponding to the total energy of the biphoton (for the case of SPDC generation, σ_p is the bandwidth of the pump photon that generates the biphoton), σ_{DC} is the bandwidth for the allowed signal-idler splittings (corresponding to the phase-matching bandwidth for the SPDC process), and N is chosen so that $\int |\phi(k_1, k_2)|^2 dk_1 dk_2 = 1$.

The correlation parameter $s = \sigma_{\text{DC}}/\sigma_p$ can be used to quantify the amount of correlations in the biphoton state, with $s = 0$ corresponding to classical uncorrelated light and $s \rightarrow \infty$ for perfect energy anticorrelation.[1] In this case, Eq. (2) reduces to

$$\phi(k_1, k_2) = N \exp\left[-\frac{(\Delta k - \Delta\bar{k})^2}{2\sigma_{\text{DC}}^2}\right] \delta(\Sigma k - \Sigma\bar{k})$$

$$\times \exp\left[-\frac{i}{\hbar}(t_1 k_1 + t_2 k_2)\right]. \tag{3}$$

B. Interaction Hamiltonian

The interaction Hamiltonian used is given as in [19]:

$$\hat{H} = \int_k dk \, k \, a_k^\dagger a_k + \sum_\nu \omega_{i_\nu} |i_\nu\rangle \langle i_\nu| + \sum_\mu \omega_{f_\mu} |f_\mu\rangle \langle f_\mu|$$

$$+ \sum_\nu \int_k dk \sqrt{\frac{g_{gi} F_{g,\nu}}{\pi}} |i_\nu\rangle \langle g| a_k + \text{H.c.}$$

$$+ \sum_{\nu,\mu} \int_k dk \sqrt{\frac{g_{if} F_{\nu,\mu}}{\pi}} |f_\mu\rangle \langle i_\nu| a_k + \text{H.c.} \tag{4}$$

The first line includes the diagonal terms for photon and vibrational state energies. The second and third line represent the ground- to intermediate-state and intermediate- to final-state coupling, where g_{gi} and g_{if} are the spontaneous emission rates for the transitions and $F_{\nu,\mu}$ and $F_{g,\nu}$ are the Franck-Condon factors between the vibronic levels of the different electronic states.

The time evolution of the system can be obtained from Eq. (4) as

$$|\Psi(t)\rangle = \exp\left[-\frac{i}{\hbar}\hat{H}t\right] |\Psi(0)\rangle \tag{5}$$

where the initial state $|\Psi(0)\rangle$ is given by

$$|\Psi(0)\rangle = \int \phi(k_1, k_2) |k_1, k_2\rangle \otimes |g\rangle \, dk_1 dk_2. \tag{6}$$

Equation (5) is solved by discretization and numerical diagonalization [32] of the Hamiltonian $\hat{H}$.

---

[1]That is, $\sigma_p \rightarrow 0$ and $\delta(\Sigma k - \Sigma\bar{k}) = 0$.
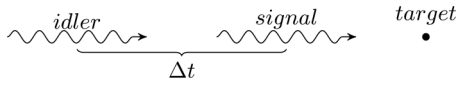
FIG. 2.   Schematic picture of the TPA process: the two incident photons interact with the target molecule sequentially with a controllable time delay Δt between them.

C. Two-photon absorption

The overall TPA process can be regarded as the superposition of many discrete transition pathways between vibronic levels, each one corresponding to a specific couple of intermediate and final vibronic states $|i_\nu\rangle$ and $|f_\mu\rangle$. Each pathway is therefore identified by a signal energy, corresponding to the energy of the $|g\rangle \rightarrow |i_\nu\rangle$ transition, and by a idler energy corresponding to the $|i_\nu\rangle \rightarrow |f_\mu\rangle$ transition. The sequence of pulses with controlled delay Δt is given in Fig. 2. If the biphoton spectrum allows for the excitation of more than one pathway, all excited pathways will interfere to collectively construct the final-state population.

Figure 3 shows the biphoton spectrum with the various excitation pathway energies superimposed, for both uncorrelated and correlated biphotons.

III. RESULTS AND DISCUSSION

A. Population dynamics in the two regimes

As shown in Fig. 4, the effects of correlations in the biphoton can be immediately seen in the excited-state population dynamics. In the uncorrelated case, the broadband nature of the photons leads to a narrow temporal distribution [Fig. 4(a)]: the arrival time of both photons is well defined, which is signified by the sharp increases in the intermediate- and final-state population corresponding to the arrivals of the signal and idler photon, respectively.

The use of SPDC as a source allows for independent control of $\sigma_{\rm DC}$ and σ_p (by controlling the phase matching and the pump bandwidth, respectively), giving an additional parameter to two-photon spectroscopy [33]. Therefore, for the correlated case, even if each individual photon maintains a broadband marginal spectrum, the total energy of the biphoton
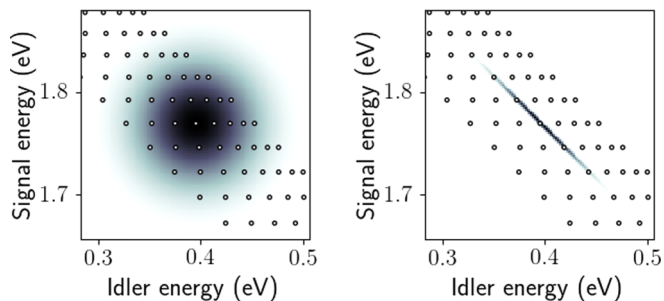

FIG. 3.   Uncorrelated (left, correlation strength $s = 1$) and correlated (right, correlation strength $s = 30$) biphoton wave functions compared to the energies of the various excitation pathways. Every dot represents a signal-idler combination corresponding to a TPA transition through specific intermediate- and final-state vibronic levels. Pathways lying on each negative slope diagonal lead to the same final vibronic level through different intermediate vibronic levels.
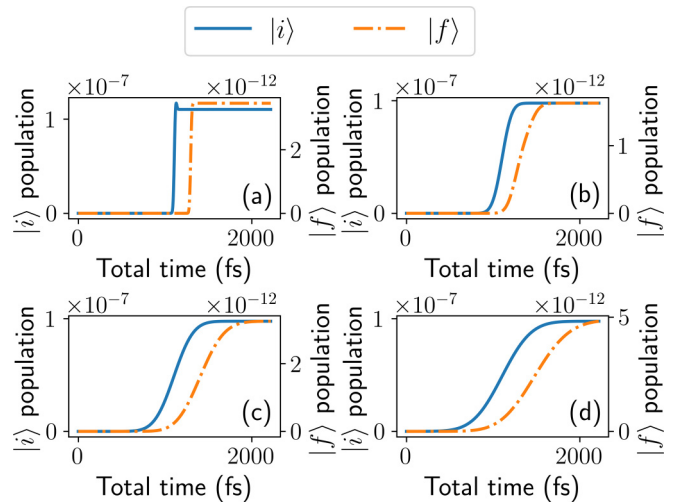

FIG. 4.   Population dynamics of $|i\rangle$ and $|f\rangle$ states for different correlation strengths of the biphoton spectrum: (a) $s = 1$, (b) $s = 10$, (c) $s = 20$, and (d) $s = 30$. The uncorrelated case $s = 1$ shows sharp edges corresponding to the arrival of the photons on the sample, while for the correlated cases a gradual increase in population is observed for both states.

is narrow band (high s corresponds to low σ_p), causing a large uncertainty in the biphoton arrival time. This leads to a systematic elongation of the intermediate- and final-state population buildup from Fig. 4(a) to Fig. 4(d). However, since the down conversion bandwidth $\sigma_{\rm DC}$ is not affected by the correlations, the correlated biphoton maintains the information on the signal-idler delay, with the $|f\rangle$ state population lagging behind $|i\rangle$ by the fixed delay time $\Delta t = t_2 - t_1$ as can be seen in all graphs in Fig. 4.

B. Effect of energy correlations

In a classical pump-probe setup, the broadband nature of the pump and probe pulses leads to the excitation of multiple transition pathways, with the result of many vibronic levels in the final state being populated. As shown in Eq. (3), the use of a SPDC source allows for fine control of the joint spectral distribution, so that only the pathways leading to a single "target" vibronic level $|f_\nu\rangle$ ($\nu = 3$ has been used in this paper) are excited.

This allows the SPDC generated light to show high spectral selectivity while maintaining a large down conversion bandwidth $\sigma_{\rm DC}$. Figure 5 presents the effects of correlation strength on population yield (i.e., the final-state population integrated over all levels as evaluated at the end of the time evolution) by introducing a final-state selectivity measure $\mathcal{S}_\nu = \sum_\mu \frac{|\langle f_\nu|f_\nu\rangle|^2}{|\langle f_\mu|f_\mu\rangle|^2}$ that compares the amount of population in the targeted vibronic level to the total excited population in the electronic state.

For weak correlations, the observed behavior is highly dependent on the relative transition probabilities between all excited pathways (see Fig. 3). In this instance, the high total population yield (blue line) can be attributed to the excitation of the final state through pathways that have higher Franck-Condon factors than the targeted excitation. Those pathways
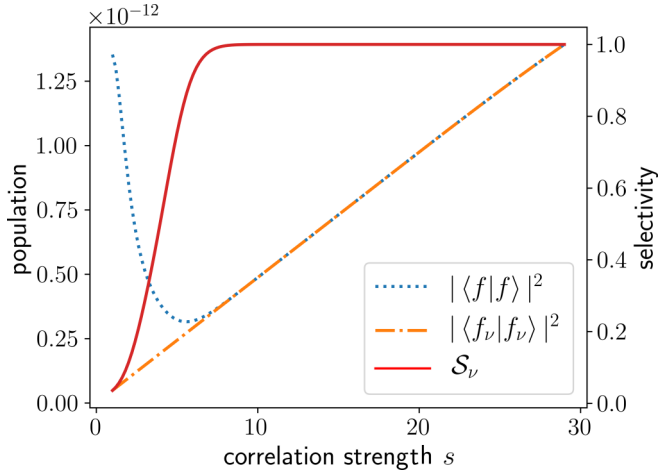
FIG. 5. Final-state selectivity as a function of correlation parameter, with results shown for target final vibronic state $\nu = 3$ and delay $\Delta t = 0$. The overall population $|\langle f|f \rangle|^2$ shows an initial drop as correlations increase, which is then offset by the linear growth of the target state population $|\langle f_\nu|f_\nu \rangle|^2$. This causes the selectivity $\mathcal{S}_\nu$ to quickly rise to 1, signifying that for high correlation strengths all the excited population is in the targeted state.

FIG. 6. Final-state population as a function of signal-idler delay. Correlated results are shown for $s = 30$ and uncorrelated for $s = 1$. The correlated photons show the same time resolution as the uncorrelated one, with a slightly higher yield. It is important to notice that the contribution to the correlated yield comes from a single vibronic state.

excite vibronic levels different from the target level, and are quickly suppressed as s increases.

For strongly correlated biphoton states, all the available energy is concentrated in the pathways leading to the excitation of the targeted vibronic state $|f_\nu\rangle$. This in turn is responsible for high selectivity and high yield.

C. Effect of time correlations

The enhanced energy selectivity demonstrated in the previous section does not result in a reduced time resolution for the signal-idler delay, as the down conversion bandwidth σ_{DC} can be controlled independently from the correlation strength $s = \sigma_{DC}/\sigma_p$.

This can be demonstrated by looking at the yield vs delay relation (i.e., the pump-probe spectrum) for the TPA process. The pump-probe spectrum for both the correlated and uncorrelated cases can be obtained by calculating the final-state population $|\langle f|f \rangle|^2$ present at the end of the time evolution as a function of the delay Δt between the signal and idler photons.

Figure 6 shows a modulation in the pump-probe spectrum oscillations reflecting the intermediate-state $|i\rangle$ vibrational dynamics. The large peaks are due to $|i\rangle \rightarrow |f\rangle$ transitions at the inner turning point of the wave packet; the smaller peaks at half periods are due to transitions at the classical outer turning point of the potential well.

While the overall yields of the uncorrelated and correlated cases are similar, it is important to notice that in the first case the population is divided among many vibronic levels, while in the second case all the population is in the targeted vibronic level (cf. $s = 1$ and 30 in Fig. 5). This observation also explains the different shapes of the two signals, i.e., the reduced amplitude of the outer turning point peak in the uncorrelated pump-probe spectrum and the different oscillation periods.
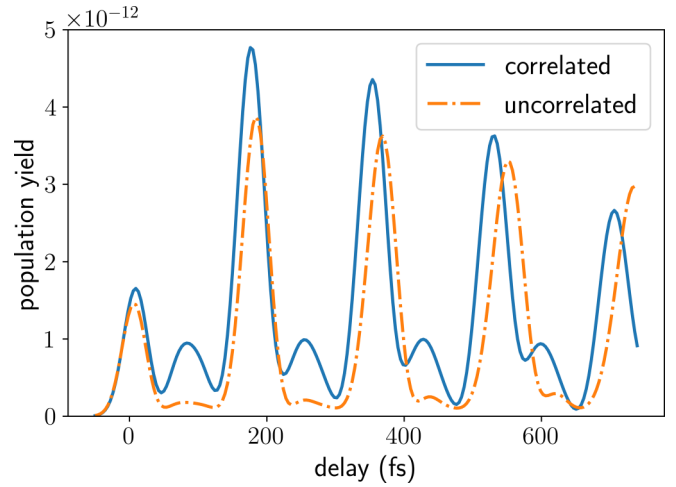
For the first, it must be noted that the targeted vibrational state shows a comparatively high transition probability at the outer turning points of the wave packet compared to final levels with $\nu > 3$. This is due to the confinement of the excited wave packet to regions that are ideally covered by the targeted level $\nu = 3$. The wave packet in $|i\rangle$ does not reach out to internuclear distances, where the $\nu > 3$ levels show optimal Franck-Condon factors at the outer turning point. The uncorrelated case uses all Franck-Condon factors possible within the bandwidth, and thus shows less modulation at the outer turning point. At the inner turning point, all final level vibrational wave functions are confined to the same region in space. Therefore, the inner turning points are similar in the correlated and uncorrelated cases.

Regarding the difference in oscillation period, the explanation is found in the anharmonicity of the final state, where transitions to each vibronic level have different periods. Since the uncorrelated signal consists of contributions to different final vibronic states, it shows a superposition of oscillations with diverse periodicity.

The selectivity afforded by the use of correlated photons allows for the study of the oscillation dynamics belonging to every individual final level. As each level possesses a different "probe window" (i.e., a region where the density is free of nodes), a systematic study of the oscillation dynamics for many target levels would give information about the anharmonicity of the $|i\rangle$ state, by sampling the potential well at different locations.

As shown in Fig. 7, by restricting the evaluation of the pump-probe spectrum to the targeted vibronic state we observe no differences in the oscillation period and outer turning point behavior for correlated vs uncorrelated light.

D. Yield improvement through spectral shaping

Further improvement on the overall yield of the process can be obtained by shaping the incoming biphoton spectrum
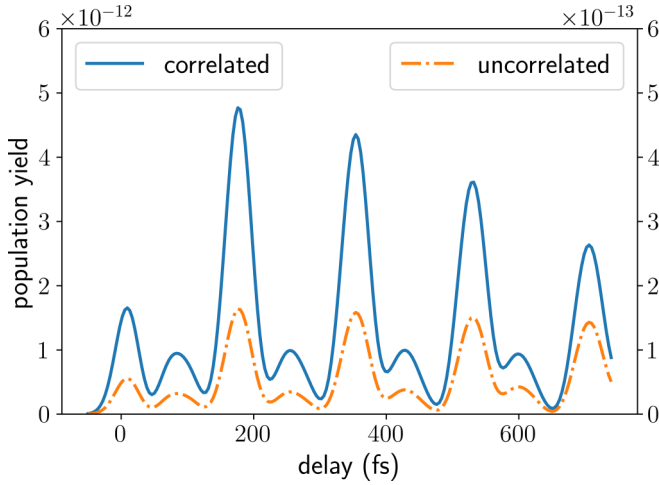
FIG. 7. Final-state population marginal of the targeted vibronic state only for correlated ($s = 30$, left axis scale) and uncorrelated ($s = 1$, right axis scale) photons. The outer turning point feature is present in both and there is no mismatch in the oscillation period.

to match the targeted excitation pathways in the molecule. This allows for all the available energy to be concentrated exclusively in the spectral regions where it can be absorbed. This can be accomplished by the coherent superposition of different narrow-band sources, with each source tuned to a different excitation pathway. Such a biphoton wave function is plotted in Fig. 8 and can be represented as [cf. Eq. (2)]

$$\phi(k_1, k_2) = N \sum_{\nu} \exp\left[-\frac{(k_1 - k_{1\nu})^2 + (k_2 - k_{2\nu})^2}{2\sigma^2}\right]$$

$$\times \exp\left[-\frac{i}{\hbar}(t_1 k_1 + t_2 k_2)\right]. \quad (7)$$

Figure 9 shows how using an appropriately shaped biphoton state can dramatically improve yield without affecting the signal-idler delay resolution. The different structure of the half-period peaks with respect to Fig. 6 is to be attributed to
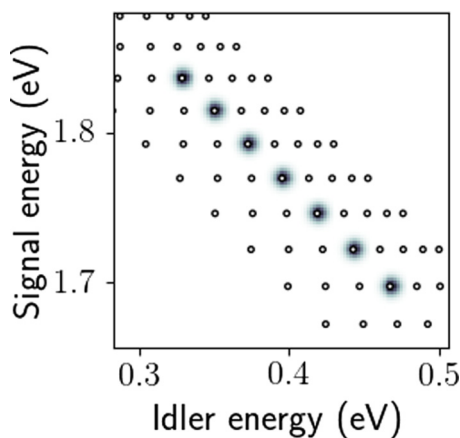

FIG. 8. Biphoton state with the spectrum designed to maximize population yield in the targeted final state. As in Fig. 3, every dot represents a signal-idler combination corresponding to a TPA transition through specific intermediate- and final-state vibronic levels.
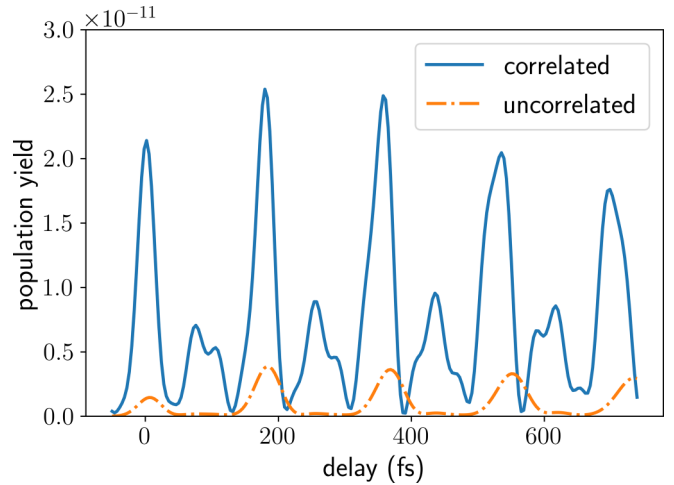

FIG. 9. Yield comparison between uncorrelated and shaped biphoton states. The shaped state shows population yield one order of magnitude larger than that of the uncorrelated case.

the different distributions of the energies between the various excitation pathways (i.e., gaussian vs flat), resulting in a different interference pattern.

The linear dependence of yield vs correlation strength shown in Fig. 5 together with the results of this section indicate that the higher yield shown by the correlated photons is to be explained by the larger overlap of the correlated biphoton spectrum with the absorption spectrum of the sample.

IV. CONCLUSIONS

In this paper, we studied the effects of time-energy correlations on SPDC-generated biphotons when used for time-resolved two-photon spectroscopy. We investigated the dependence of final-state selectivity and yield on correlation strength and showed that the yield of the correlated two-photon process scales linearly within the studied range. Moreover, we demonstrated that the increase in spectral selectivity does not lead to a decrease in time resolution of the biphoton delay. We interpret our results in an intuitive fashion, using the overlap between the two-photon spectrum with the vibrational transitions in k_1 k_2 space. Within that framework, we can easily explain differences in the pump-probe spectra for changing correlation by the involvement of transitions with different Franck-Condon factors and vibrational periodicity. Finally, we propose an excitation scheme that significantly increases yield by a more efficient use of the available power.

ACKNOWLEDGMENT

APPENDIX: SIMULATION PARAMETERS

As described in Secs. II A and II B, the modeled molecular system is described as a collection of Morse oscillators, one for each electronic state. The potential-energy surfaces for the

TABLE I. Parameters for the different potentials of ICl used in this study.

	T_e (cm^{-1})	ω_e (cm^{-1})	$\omega_e \chi_e$ (cm^{-1})	r_e (Å)
$|g\rangle$	0	384.3	1.50	2.319
$|i\rangle$	13742	212.3	2.39	2.692
$|f\rangle$	17363	221.1	9.62	2.657

internuclear distance in each state are constructed as follows:

$$V(r) = T_e + D_e(1 - e^{-a(r-r_e)})^2 \qquad (A1)$$

where D_e and a are related to the spectroscopic constants ω_e and $\omega_e \chi_e$ through [34]

$$D_e = \frac{\hbar \omega_e^2}{4 \omega_e \chi_e}, \qquad a = \omega_e \sqrt{\frac{\mu}{2D_e}} \qquad (A2)$$

where $\mu = 27.7$ amu is the reduced mass of the system and the spectroscopic constants for the relevant states are given in Table I [26]. The Franck-Condon factors are then calculated using the vibrational eigenstates $|e_i\rangle$ of the potentials obtained from Eq. (A2) as $F_{i,j} = |\langle e_i | e_j \rangle|^2$.

The square roots of the Franck-Condon factors used in this paper are plotted in Fig. 10. It is useful to notice that since
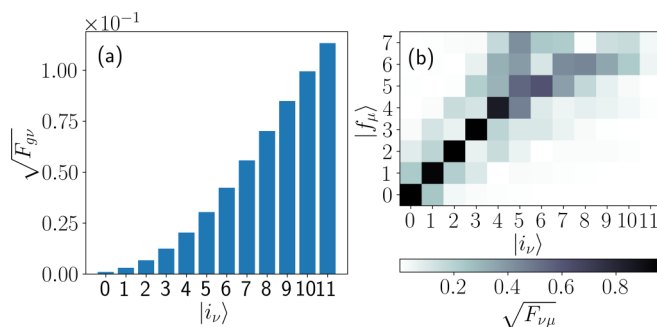

FIG. 10. Roots of the Franck-Condon factors for $|g\rangle \rightarrow |i\rangle$ (a) and $|i\rangle \rightarrow |f\rangle$ (b) transitions. The large difference in the equilibrium position r_e between the $|g\rangle$ and $|i\rangle$ states suppresses the transition probability for low vibronic states in panel (a). In panel (b) the values cluster around the diagonal. This is due to the similar shape of the $|i\rangle$ and $|f\rangle$ states, enhancing transitions that do not change vibrational kinetic energy. The clustering is less pronounced at high energies due to the different anharmonicities of the two states.

the effects of correlations arise as a consequence of coherent interference between the complex amplitudes of the different vibronic states the relevant parameter is $\sqrt{F_{i,j}}$ (as opposed to $F_{i,j}$).

[1] A. H. Zewail, Pure Appl. Chem. **72**, 2219 (2000).

[2] S. Mukamel, *Principles of Nonlinear Optics and Spectroscopy* (Oxford University, New York, 1995).

[3] R. W. Boyd, *Nonlinear Optics* (Academic, New York, 2008).

[4] J. Javanainen and P. L. Gould, Phys. Rev. A **41**, 5088 (1990).

[5] B. Dayan, A. Pe'er, A. A. Friesem, and Y. Silberberg, Phys. Rev. Lett. **93**, 023005 (2004).

[6] O. Varnavski, B. Pinsky, and T. Goodson, J. Phys. Chem. Lett. **8**, 388 (2017).

[7] P. G. Kwiat, K. Mattle, H. Weinfurter, A. Zeilinger, A. V. Sergienko, and Y. Shih, Phys. Rev. Lett. **75**, 4337 (1995).

[8] K. E. Dorfman, F. Schlawin, and S. Mukamel, Rev. Mod. Phys. **88**, 045008 (2016).

[9] S. Carrasco, M. B. Nasr, A. V. Sergienko, B. E. Saleh, M. C. Teich, J. P. Torres, and L. Torner, Opt. Lett. **31**, 253 (2006).

[10] B. E. A. Saleh, B. M. Jost, H.-B. Fei, and M. C. Teich, Phys. Rev. Lett. **80**, 3483 (1998).

[11] R. K. Burdick, O. Varnavski, A. Molina, L. Upton, P. Zimmerman, and T. Goodson, J. Phys. Chem. A **122**, 8198 (2018).

[12] J. Svozilík, J. Peřina, and R. de J. León-Montiel, J. Opt. Soc. Am. B **35**, 460 (2018).

[13] F. Schlawin and A. Buchleitner, New J. Phys. **19**, 013009 (2017).

[14] F. Schlawin, K. E. Dorfman, and S. Mukamel, Acc. Chem. Res. **51**, 2207 (2018).

[15] F. Schlawin and S. Mukamel, J. Chem. Phys. **139**, 244110 (2013).

[16] A. Eshun, Z. Cai, M. Awies, L. Yu, and T. Goodson, J. Phys. Chem. A **122**, 8167 (2018).

[17] J. P. Villabona-Monsalve, O. Calderón-Losada, M. N. Portela, and A. Valencia, J. Phys. Chem. A **121**, 7869 (2017).

[18] J. P. Villabona-Monsalve, O. Varnavski, B. A. Palfey, and T. Goodson, J. Am. Chem. Soc. **140**, 14562 (2018).

[19] H. Oka, J. Chem. Phys. **135**, 164304 (2011).

[20] H. Oka, J. Chem. Phys. **134**, 124313 (2011).

[21] H. Oka, Phys. Rev. A **81**, 053837 (2010).

[22] H. Oka, Phys. Rev. A **97**, 033814 (2018).

[23] F. Schlawin, K. E. Dorfman, B. P. Fingerhut, and S. Mukamel, Phys. Rev. A **86**, 023851 (2012).

[24] J. Svozilík, J. Peřina, and R. de J. León-Montiel, Chem. Phys. **510**, 54 (2018).

[25] R. d. J. León-Montiel, J. Svozilík, J. P. Torres, and A. B. U'Ren, Phys. Rev. Lett. **123**, 023601 (2019).

[26] K. P. Huber and G. H. Herzberg (data prepared by Jean W. Gallagher and Russell D. Johnson III), Constants of diatomic molecules, NIST chemistry webbook, NIST standard reference database 69 (retrieved 10 October 2019).

[27] F. Sizov and A. Rogalski, Prog. Quantum Electron. **17**, 93 (1993).

[28] L. Esaki, IEEE J. Quantum Electron. **22**, 1611 (1986).

[29] D. Bimberg and U. W. Pohl, Materials Today **14**, 388 (2011).

[30] N. N. Ledentsov, V. M. Ustinov, V. A. Shchukin, P. S. Kop'ev, Z. I. Alferov, and D. Bimberg, Semiconductors **32**, 343 (1998).

[31] W. G. Brown and G. E. Gibson, Phys. Rev. **40**, 529 (1932).

[32] R. B. Lehoucq, D. C. Sorensen, and C. Yang, *ARPACK Users Guide* (Society for Industrial and Applied Mathematics, Philadelphia, 1998).

[33] B. Dayan, A. Pe'er, A. A. Friesem, and Y. Silberberg, arXiv:quant-ph/0302038 (2003).

[34] J. P. Dahl and M. Springborg, J. Chem. Phys. **88**, 4535 (1988).